Improving the statistical analysis of antihydrogen free fall by using near-edge events

Olivier Rousselle,[1] Pierre Cladé,[1,*] Saïda Guellati-Khélifa,[1,2] Romain Guérout,[1] and Serge Reynaud[1]
[1]*Laboratoire Kastler Brossel, Sorbonne Université, CNRS, ENS-PSL, Collège de France, 4 place Jussieu, 75005 Paris, France*
[2]*Conservatoire National des Arts et Métiers, 292 rue Saint Martin, 75003 Paris, France*

(Received 22 November 2021; accepted 26 January 2022; published 22 February 2022)

An accurate evaluation of the gravity acceleration from the timing of free fall of antihydrogen atoms in the Gravitational Behaviour of Anti-hydrogen at Rest (GBAR) experiment requires one to account for obstacles surrounding the antimatter source. These obstacles reduce the number of useful events but may improve accuracy since the edges of the shadows of obstacles on the detection chamber depend on gravity, bringing additional information about the value of g. We perform Monte Carlo simulations to obtain the dispersion and give a qualitative understanding of the results by analyzing the statistics of events close to an edge. We also study the effect of specular quantum reflections of antihydrogen on surfaces and show that they do not degrade the accuracy that much.

DOI: 10.1103/PhysRevA.105.022821

I. INTRODUCTION

One of the fascinating questions which remain open in modern physics is the asymmetry between matter and antimatter observed in the universe but not fully accounted for in the standard model [1–4]. In particular experimental tests of the effect of gravity on antimatter must still be improved [5]. Ambitious projects are currently being developed at new CERN facilities to produce low-energy antihydrogen ($\overline{\mathrm{H}}$) atoms [6] and measure $\bar{g}$, the gravity acceleration of neutral $\overline{\mathrm{H}}$ atoms [7–9]. Among these projects, the Gravitational Behaviour of Anti-hydrogen at Rest (GBAR) experiment aims at a relative accuracy of 1% on $\bar{g}$ by timing the free fall of ultracold $\overline{\mathrm{H}}$ atoms [10,11]. Knowing the sign and order of magnitude of $\bar{g}$ would already be an important achievement, and improving the accuracy of its measurement would be crucial for advanced tests of the equivalence principle along the line of the many high-precision tests performed on matter objects [12–16].

The principle of the GBAR experiment is based upon an original idea of Walz and Hänsch [17]. Antihydrogen ions $\overline{\mathrm{H}}^+$ are cooled in an ion trap by using laser-cooling techniques. The excess positron is photodetached with a laser, forming a neutral antihydrogen atom $\overline{\mathrm{H}}$, with the laser pulse marking the start of the free fall. The end of free fall is timed by the annihilation of $\overline{\mathrm{H}}$ on the detection surface, and the acceleration $\bar{g}$ is deduced from a statistical analysis of annihilation events. In a previous work [18], we analyzed the accuracy of $\bar{g}$ to be expected in a simple geometry for the GBAR experiment, taking into account the impact of the photodetachment process on the initial velocity distribution and the statistics of annihilation events. We also noticed that the accuracy could be improved by considering the ceiling that intercepts some of the trajectories.

In the present paper, we go further in this analysis by taking into account the obstacles surrounding the antihydrogen source, required for the experiment [19,20]. These obstacles, such as the electrodes of the ion trap, intercept some trajectories of $\overline{\mathrm{H}}$ atoms. As for the ceiling in [18], one might think that it degrades the accuracy as it reduces the number of annihilation events used for the measurement. We show that the opposite happens, with the accuracy of the measurement of $\bar{g}$ improved thanks to the additional information gained from events close to the edges of the shadow of obstacles.

We will first specify the geometry (Sec. II) and present a detailed simulation of annihilation events in the presence of obstacles to calculate the dispersion of the free-fall measurement (Sec. III). We will then provide a qualitative understanding of the results by analyzing the statistics of events close to an edge of the shadow of obstacles (Sec. IV). We will finally make the analysis more complete by evaluating the effect of quantum reflection of $\overline{\mathrm{H}}$ atoms on the Casimir-Polder potential in the vicinity of matter surfaces [21]. Including this effect in the statistical analysis of the experiment, we will show that quantum reflection does not degrade the accuracy that much (Sec. V). We assume quantum reflection is specular, which requires the surfaces exposed to antiatoms to be well polished.

II. GEOMETRY OF THE EXPERIMENT

The source of $\overline{\mathrm{H}}$ atoms is placed at the center of the cylindrical vacuum chamber (radius R_c and free-fall height H_f) in which the free-fall measurement is performed. This source is surrounded by obstacles such as the electrodes of the trap [19,20]. We define a cleaner geometry by hiding obstacles with two symmetrically positioned disks of radius R_d placed above and below the trap at a distance H_d. The resulting geometry is shown schematically in Fig. 1, with trajectories to the surfaces of the chamber represented as blue lines [21].

The symmetrical configuration produces a simple geometry which will be more easily studied in Monte Carlo simulations of the experiment. We will work with a horizontal

*Corresponding author: pierre.clade@lkb.upmc.fr

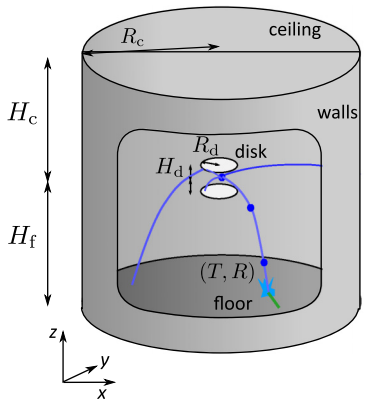

FIG. 1. Schematic representation of the GBAR free-fall chamber with two disks symmetrically positioned above and below the trap to mask the obstacles surrounding it. Trajectories to the surfaces of the chamber are represented as blue lines.

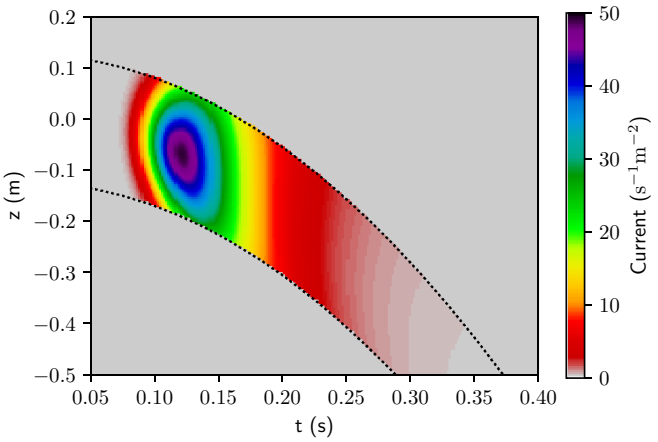

FIG. 2. Distribution of annihilation events $j(\mathbf{R}, t)$ (in $s^{-1}\,m^{-2}$) on the wall as a function of t and position $(X = 0, Y = R, Z)$ with two disks. Parameters are $R_d = 2$ cm, $H_d = 1$ cm, $R_c = 25$ cm, $f = 1$ MHz, and $\delta E = 30$ μeV.

polarization of the photodetachment laser in order to launch the atoms preferably in the free interval between the two disks [18]. In the first part of the study we will generate random events mimicking the forthcoming experiment with a reference value $g_0 = 9.81\ \mathrm{m/s^2}$. In the second part, we will present the statistical analysis of these events mimicking the data analysis process to be developed at a later stage of the experiment. The whole analysis will be done in a manner quite analogous to that presented in [18], with, however, important differences discussed now.

The evaluation of g from the analysis of annihilation data involves the calculation of the probability current $J(\mathbf{R}, T)$ (number per unit of surface and unit of time) to detect a particle at position $\mathbf{R}$ in space and T in time. In [18], we detailed the calculation of the same quantity $J_0(\mathbf{R}, T)$ while ignoring the presence of obstacles. In the presence of symmetrical disks, in contrast, the reasoning has to consider separately the annihilation events on the surfaces of the free-fall chamber, which are used for estimating g, and those on the disks, which contain essentially no information on g. Hence, we will be mainly interested in the current on the surfaces of the free-fall chamber with a probability integral P_c smaller than 1. In the following we fix the initial number N of atoms, but our analysis of dispersion accounts for the fact that the number of events $N_c = NP_c$ detected on the surfaces of the chamber is smaller than N.

At the end of the calculations, we will obtain the mean μ_g and the standard deviation σ_g of the estimator defined for $\overline{g}$, simply denoted g from now on. In spite of the loss of useful events, it will turn out that the standard deviation σ_g may be smaller in the presence of the obstacles. The main reason for this important result can already be understood by looking at the detection current on the walls of the free-fall chamber represented in Fig. 2. One clearly sees the sharp boundaries of the shadow induced on the walls by the presence of the disks. The position in space and time of this shadow depends on the value of g, and its detection allows us to gain information on the value of g.

The dispersion of the initial position of the ion in the trap plays a negligible role in the problem, while the dispersion of the photodetachment time t_0 has to be accounted for as in [18]. The time of the annihilation event T is $t + t_0$, where t is the time of flight and t_0 is the precise time of the photodetachment event. Hence, the current $J(\mathbf{R}, T)$ (taking into account the dispersion on t_0) is calculated as the convolution of a current $j(\mathbf{R}, t)$ neglecting this dispersion and the distribution of t_0, assumed to be a logistic distribution with width τ,

$$J(\mathbf{R}, T) = \int j(\mathbf{R}, T - t_0)\, \delta_\tau(t_0)\, dt_0,$$
$$\delta_\tau(t_0) = \frac{1}{4\tau} \frac{1}{\cosh^2\left(\frac{t_0}{2\tau}\right)}. \quad (1)$$

The current plotted in Fig. 2 was calculated before the convolution, and the latter will round up the edges of the shadow zone without suppressing the gain of information associated with them. Currents calculated before and after the convolution on a cut with fixed altitude ($z = -0.17$ cm) are represented in Fig. 3. The effect of the dispersion on t_0, calculated here for $\tau = 500$ μs, is visible at the steps of the current corresponding to edges of the shadow of the disks. We will see that it plays an important role in some forthcoming calculations, while it can be neglected in other ones.

III. DISPERSION OF THE ESTIMATOR

In this section, we present Monte Carlo simulations to discuss the dispersion that should be expected on the measurement of g with the obstacles taken into account. We rapidly go over steps which were already discussed in [18] for the case without obstacles and discuss mainly the differences with that case.

Considering a draw of N $\overline{\mathrm{H}}$ atoms that escape from the trap after the photodetachment process, we calculate the trajectory that depends on the random initial velocity $\boldsymbol{v}_0$ and the random time of photodetachment t_0 and deduce the annihilation position in space $\mathbf{R}_i$ and time T_i. Trajectories hitting the disk

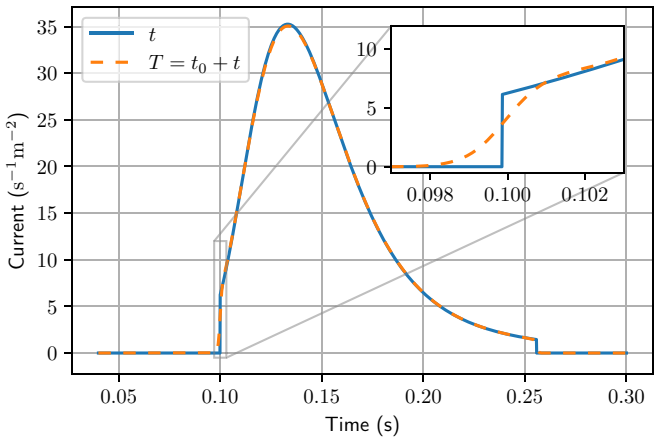

FIG. 3. Comparison between the currents $j(\mathbf{R}, t)$ and $J(\mathbf{R}, T)$ for $z = -17$ cm calculated with the same parameters as in Fig. 2; the first one is before the convolution (blue solid line), and the second one is after the convolution with $\tau = 500$ μs (orange dashed line). The effect of the dispersion on t_0 is visible on the edges of the shadow zone induced by the obstacles.

lead to annihilation there and are discarded from the forthcoming analysis as they contain no useful information on the value of g.

We thus calculate the likelihood function $\mathcal{L}$ and normalized likelihood function ℓ for the draw of N_c events that annihilate on the surfaces of the chamber,

$$\mathcal{L}(g) = \prod_{i=1}^{N_c} J(\mathbf{R}_i, t_i), \quad \ell(g) = \frac{\mathcal{L}(g)}{\int \mathcal{L}(g) dg}. \tag{2}$$

Normalized likelihood functions $\ell(g)$ are represented in Fig. 4 for a given set of parameters ($R_d = 2$ cm, $H_d = 1$ cm, $R_c = 25$ cm, $f = 1$ MHz, $\delta E = 30$ μeV) and four values of N. The different functions $\ell(g)$ plotted for each case are calculated for independent random draws.

For $N = 10$ and $N = 100$, the likelihoods are mostly flat with sudden drops to zero. This behavior is due to the obstacles and can be qualitatively understood with $\tau = 0$. Let us consider an impact at $\mathbf{R}, t$ reached by an atom for $g = g_0$. If this impact is close to an edge of the allowed area, it may fall in the shadow zone for a different value $g \neq g_0$, so that the likelihood drops to zero. The drop to zero is rounded up by the dispersion τ, with the rounding being negligible for $N = 10$ or $N = 100$ but starting to become noticeable for $N = 1000$. For $N = 10\,000$, the likelihoods are closer to Gaussian functions because the numerous annihilation events produce an efficient sampling of the rounded step.

Although all likelihood functions are centered around the expected value g_0, their maximum will fall on either side

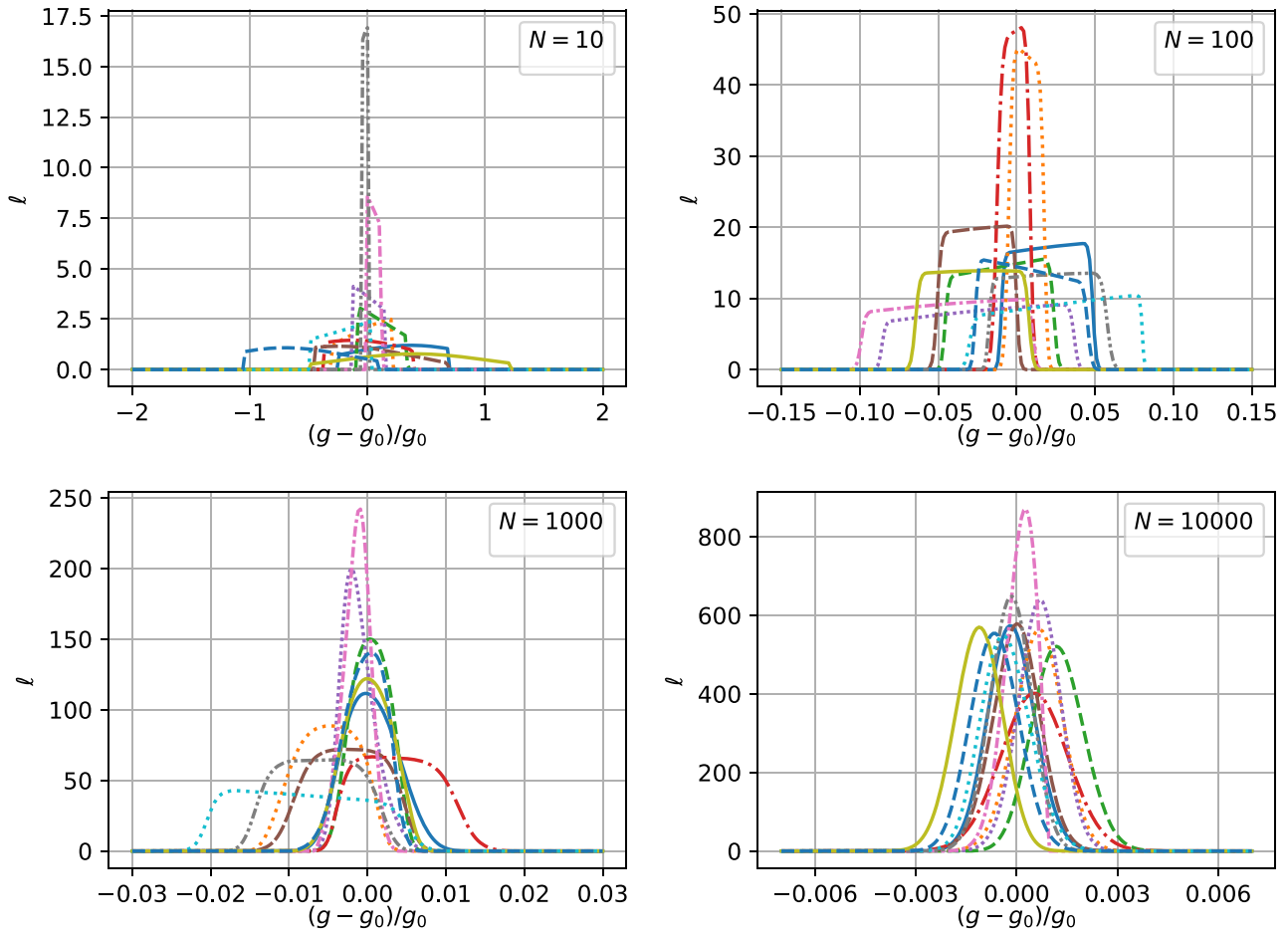

FIG. 4. Set of normalized likelihoods $\ell(g)$ for different values of the initial number of atoms N. The parameters are the same as in Fig. 3.

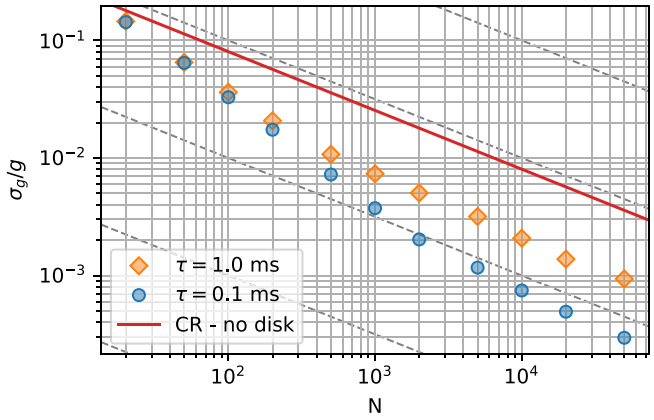

FIG. 5. Relative dispersion obtained with Monte Carlo simulation of the experiment with two disks. Orange diamonds and blue circles represent, respectively, the dispersion for $\tau = 1$ ms and $\tau = 0.1$ ms. The red solid line is the Cramer-Rao limit without disks. The light gray lines are guides for the eye showing a $1/\sqrt{N}$ scaling.

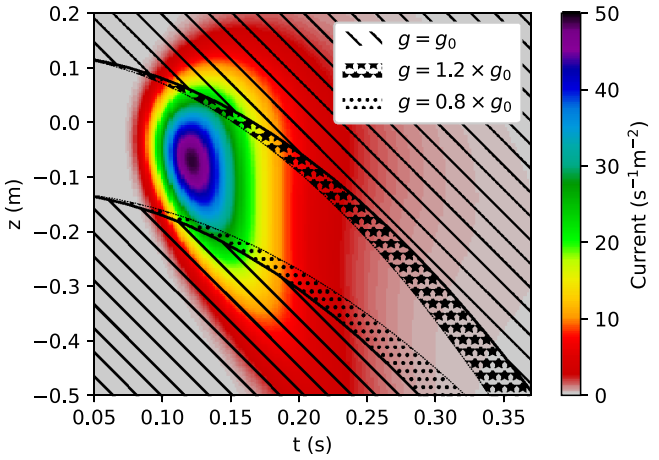

FIG. 6. Current j as a function of the altitude z and time of flight t. The area with diagonal hatching represents the shadow from the two disks for g_0. The two dotted areas represent zones that are not in the shadow for $g = g_0$ but are in the shadow for $g = 1.2g_0$ and $g = 0.8g_0$. The probability of having an impact in this area corresponds to $F_{\max}(1.2g_0)$ and $F_{\min}(0.8g_0)$.

of their plateau, so that the common maximum-likelihood estimator will show large variations. In order to circumvent this problem, we define another estimator $\breve{g}$ as the mean value of the likelihood ℓ and will use it in all forthcoming simulations,

$$\breve{g} = \int g\,\ell(g)dg = \frac{\int g\,\mathcal{L}(g)dg}{\int \mathcal{L}(g)dg}. \tag{3}$$

Figure 5 shows the relative dispersion of $\breve{g}$ as a function of the number N of initial events. The dispersion of t_0 is taken into account for all calculations, although it has a small effect for a small value of N. We see that the variation of the dispersion versus N does not follow $1/\sqrt{N}$ except for very large values of N. This behavior is an indication that the statistical efficiency is reached only for those very large values. In the high-N regime the dispersion depends on τ, and it is smaller than the dispersion without the obstacles.

IV. STATISTICS OF EVENTS CLOSE TO AN EDGE

We now present two methods which are useful to understand the results of the simulations in the two regimes discussed at the end of Sec. III. These two methods deal with the statistics of events close to an edge, first in the sharp case ($\tau = 0$) better suited to small values of N and then in the rounded case ($\tau \neq 0$) better suited to large N.

A. The min-max model

We first discuss the drop in the likelihood observed for values of N such as $N = 100$. The sampling of the edges of the shadow zone is not efficient in this case, so we can neglect the dispersion τ of t_0 and simplify calculations by using the current $j(\mathbf{R}, t)$ before convolution (so that $T \equiv t$).

For a given impact $\mathbf{R}, t$, we calculate the initial velocity assuming a value of g. We define a function $\lambda_g(\mathbf{R}, t)$ that is equal to 1 if the associated trajectory reaches the detection point without hitting the disks and equal to 0 in the opposite case where $\overline{\mathrm{H}}$ is annihilated on the disks. We get the current j as the product of this function by the current j_0 calculated without obstacles,

$$j(\mathbf{R}, t) = \lambda_g(\mathbf{R}, t) j_0(\mathbf{R}, t). \tag{4}$$

For a random draw of N atoms, the likelihood function (2) is then written as

$$\mathcal{L}(g) = \mathcal{L}_0(g)\pi(g), \quad \mathcal{L}_0(g) = \prod_{i=1}^{N} j_0(\mathbf{R}_i, t_i),$$
$$\pi(g) = \prod_{i=1}^{N} \lambda_g(\mathbf{R}_i, t_i), \tag{5}$$

with $\mathcal{L}_0(g)$ being the likelihood function calculated without obstacles. Meanwhile, $\pi(g)$ is a rectangular function with a unit value on the interval between minimal and maximal values of g which are random variables depending on the full set of impact parameters for the N_c events,

$$\pi(g) = \begin{cases} 1 & \text{if } g \in [g_{\min}, g_{\max}], \\ 0 & \text{otherwise.} \end{cases} \tag{6}$$

We now calculate the statistics of $g_{\max}$, with the same method being applicable for $g_{\min}$. To this aim, we first define the following expectation taken over all possible impact parameters without obstacles:

$$F_{\max}(g) = \mathbb{E}(\lambda_{g_0}(1 - \lambda_g)), \tag{7}$$

which is the probability to be in the allowed area for g_0 and in the shadow for g. The function $F_{\max}(g)$, shown in Fig. 6, is also the cumulative distribution function of $g_{\max}$ for a single event and $f_{\max}(g) = F'_{\max}(g)$, the distribution function. For a draw of N events, the distribution of $g_{\max}$ can then be written as

$$f_{N,\max}(g) = N f_{\max}(g)[1 - F_{\max}(g)]^{N-1}. \tag{8}$$

For a large value of N and for $(g-g_0)f_{\max}(g_0) \ll 1$, the random variable $(g_{\max}-g_0)$ follows an exponential distribution of parameters $Nf_{\max}(g_0)$,

$$f_{N,\max}(g) \simeq N f_{\max}(g_0) e^{-N(g-g_0)f_{\max}(g_0)}. \tag{9}$$

The expected value of $g_{\max}$ is $g_0 + 1/[Nf_{\max}(g_0)]$, and its standard deviation is $1/[Nf_{\max}(g_0)]$.

The likelihood $\mathcal{L}$ with obstacles is the product of the likelihood $\mathcal{L}_0$ without obstacles and the rectangular function π limited by $g_{\min}$ and $g_{\max}$. The width of $\mathcal{L}_0$ scales as $1/\sqrt{N}$, while the width of π scales as $[1/f_{\max}(g_0) + 1/f_{\min}(g_0)]/N$. When the width of π dominates the final shape, the likelihood function $\mathcal{L}$ has a trapezoidal shape. By disregarding the slope of the plateau of the trapeze, we can approximate the estimator $\check{g}$ as (the label mm stands for "min-max")

$$\check{g}_{\rm mm} \equiv \frac{g_{\max}+g_{\min}}{2}. \tag{10}$$

For large enough values of N, the events that contribute to $g_{\max}$ and $g_{\min}$ are different since they correspond to events close to different edges and there is no overlap between the areas in Fig. 6 with dots and stars. When this is the case, we can assume that $g_{\max}$ and $g_{\min}$ are uncorrelated variables and thus get the following expectation and variance for the min-max estimator (10):

$$\begin{aligned}\mathbb{E}(\check{g}_{\rm mm}) &= g_0 + \frac{1}{2N}\left(\frac{1}{f_{\max}(g_0)} - \frac{1}{f_{\min}(g_0)}\right),\\ \mathbb{V}{\rm ar}(\check{g}_{\rm mm}) &= \frac{1}{4N^2}\left(\frac{1}{f_{\max}(g_0)^2} + \frac{1}{f_{\min}(g_0)^2}\right).\end{aligned} \tag{11}$$

With the two disks symmetrically positioned with respect to the center of the trap and sufficiently close to it, $f_{\max}(g_0) = f_{\min}(g_0)$, and we call this quantity $f_{\rm mm}(g_0)$. The estimator $\check{g}_{\rm mm}$ is then unbiased, and its distribution is a Laplace distribution,

$$\begin{aligned}f_{\check{g}_{\rm mm}}(g) &= \frac{1}{\sqrt{2}\sigma_{\rm mm}} e^{-\frac{|g-g_0|}{\sqrt{2}\sigma_{\rm mm}}},\\ \sigma_{\rm mm} &= \frac{1}{\sqrt{2}Nf_{\rm mm}(g_0)},\end{aligned} \tag{12}$$

where we have denoted $\sigma_{\rm mm}$ as the dispersion of $\check{g}_{\rm mm}$ which scales as $1/N$.

If the two disks are not symmetric, $f_{\min}(g_0)$ and $f_{\min}(g_0)$ are different, and the estimator is biased. The bias is smaller than the standard deviation of the estimator, and it converges to zero with the same $1/N$ scale.

B. The Cramér-Rao bound

We now discuss the cases of large values of N for which the dispersion scales as $1/\sqrt{N}$ and can be approximated by a Cramér-Rao bound [22–24]. This corresponds to the limit of an efficient sampling of the edges and requires to account for the rounding up in J of the steps in j, thanks to the dispersion τ of t_0 [see Eq. (1)].

Due to the small value of τ compared to the timescale in j, the convolution does not appreciably change the current, except in the vicinity of the steps. An approximation of J is thus given by the expressions

$$\begin{aligned}J_\tau(\mathbf{R},T) &= J_0(\mathbf{R},T)\Lambda_{\tau,g}(\mathbf{R},T),\\ \Lambda_{\tau,g}(\mathbf{R},T) &= \int \lambda_g(\mathbf{R},T-u)\delta_\tau(u)du.\end{aligned} \tag{13}$$

Using Eq. (13), one can decompose the integral giving the Fisher information as a sum of three terms,

$$\begin{aligned}\mathcal{I}_g &= \mathcal{I}_{g,1} + \mathcal{I}_{g,2} + \mathcal{I}_{g,3},\\ \mathcal{I}_{g,1} &= \int dSdT \frac{(\partial_g J_0)^2}{J_0}\Lambda_\tau,\\ \mathcal{I}_{g,2} &= \int dSdT \frac{(\partial_g \Lambda_\tau)^2}{\Lambda_\tau}J_0,\\ \mathcal{I}_{g,3} &= 2\int dSdT(\partial_g\Lambda_\tau)(\partial_g J_0).\end{aligned} \tag{14}$$

The first term, $\mathcal{I}_{g,1}$, is the Fisher integral for the current calculated without obstacles. The second term is the Fisher information added by the steps in the current j. For this term, the integrand is non-negligible only in the vicinity of the step, with the extra information arising because the position of the step depends on g.

We first calculate this integral for a single step at a time t_s. In this case, $\lambda(t) = \theta(t-t_s)$, where θ is the Heaviside function, and $\Lambda_\tau(T) = \theta_\tau(T-t_s)$, where $\theta_\tau(T) = \int_{-\infty}^{T}\delta_\tau(u)du$. Neglecting the variation of the current j_0 over the step, this integral can be obtained analytically,

$$\int dT \frac{[\delta_\tau(t_{\rm s}-T)]^2}{\theta_\tau(t_{\rm s}-T)} = \frac{1}{2\tau}. \tag{15}$$

This integral has been calculated exactly for the logistic distribution (1) of the photodetachment moment, but similar scaling laws would hold for other models with a rounded step, with the integrals being a definition of τ. Finally, $\mathcal{I}_{g,3}$ contains all other terms; it scales as τ^0 and is thus negligible with respect to $\mathcal{I}_{g,2}$.

We thus obtain a large contribution scaling as $\frac{1}{\tau}$,

$$\mathcal{I}_{g,2} \simeq \int dS \frac{J_0(t_s)}{2\tau}(\partial_g t_{\rm s})^2. \tag{16}$$

In order to ease the calculation of the large $\mathcal{I}_{g,2}$, an approximation of $\partial_g t_{\rm s}$ can be made when obstacles are close to the source and gravity can be neglected during the flight between the source and the disks, which leads to the simple relationship

$$\partial_g t_{\rm s} \simeq \frac{t_s}{2g}. \tag{17}$$

This relationship can be seen in Fig. 6, where the horizontal width of the dotted area (proportional to $\partial_g t_s$) is proportional to t.

Equation (16) gives an integral on the boundary defined by the function λ_g. It can be replaced by an integral over the volume of points that are within $\delta g/2$ from the boundary

$$\mathcal{I}_{g,2} \simeq \frac{1}{4g_0\tau}\frac{\mathbb{E}_{g_0}(t|\lambda_{g_0-\delta g/2} - \lambda_{g_0+\delta g/2}|)}{|\delta g|}. \tag{18}$$

Here the expectation used to represent the integral is taken for impacts without obstacles. Choosing an adequate value of δg,

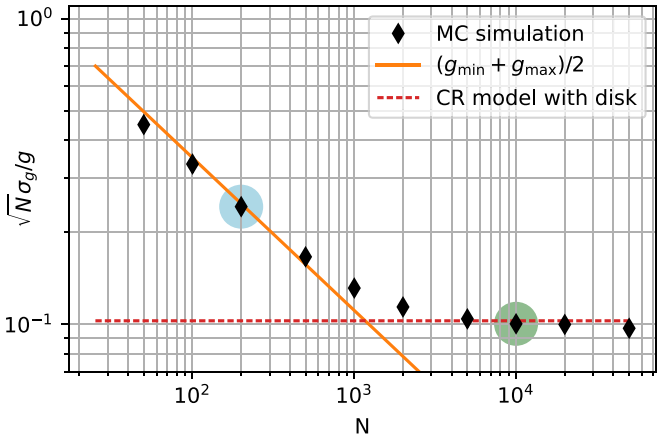

FIG. 7. Relative dispersions obtained with Monte Carlo (MC) simulations multiplied by $\sqrt{N}$ and represented versus N (black diamonds). The dashed red line represents the Cramér-Rao (CR) bound calculated with obstacles. The solid orange line is the limit given by the min-max model in Eq. (11). Results are drawn for the default configuration for the disks $R_d = 2$ cm, $H_d = 1$ cm, and $\tau = 200$ μs. The points whose normalized histograms are shown in Fig. 8 are highlighted.

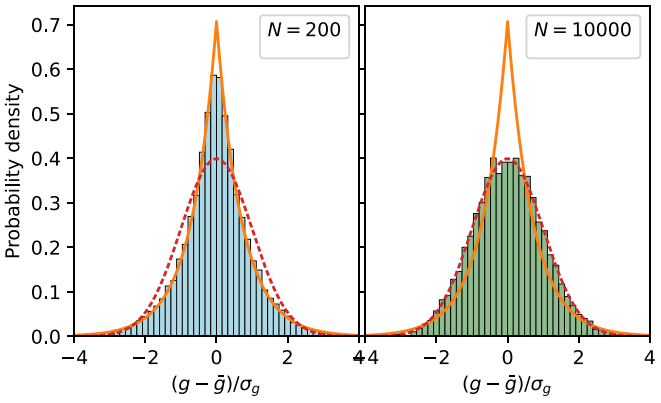

FIG. 8. Standardized histograms of $\breve{g}$ for the points $N = 200$ and 10 000 highlighted in Fig. 7. The number of draws is 50 000 for $N = 200$ and 12 000 for $N = 10\,000$. The dashed red curves represent normal distributions, a fair approximation in the limit of efficient statistics, and the solid orange curve represents Laplace distributions, a fair approximation in the min-max model.

this formula can be used to numerically calculate $\mathcal{I}_{g,2}$ with a Monte Carlo method when no analytical formula for $t_s(\mathbf{R})$ is available.

These discussions show that the large contribution $\mathcal{I}_{g,2}$ to the Fisher information is proportional to the density of events close to the step weighted by the time of flight (the longer it is, the higher is the information). Note also that the expected value is taken on both sides of the step. This formula is similar to (7), which is used to compute f_{max}, and leads to a rough relationship between the two quantities,

$$\frac{g\mathcal{I}_{g,2}}{f_{mm}} \approx \frac{\langle T \rangle}{2\tau}, \tag{19}$$

where $\langle T \rangle$ is a typical value of the time of flight R_c/v, with R_c being the radius of the chamber (see Fig. 1).

When there is more than one step at a position $\mathbf{R}$, the Fisher integral is the sum over all steps of contributions (16) or (18).

C. Discussion

In order to assess the qualitative results of the min-max and Cramér-Rao models presented in Secs. IV A and IV B, we have performed full Monte Carlo simulations of the experiment for different sets of parameters and for a simple geometry without the floor and the ceiling of the chamber so that atoms are detected only on the walls. The results of the simulation are shown in Fig. 7.

Simulations correspond to the default configuration for the disks ($R_d = 2$ cm, $H_d = 1$ cm) considered for all other figures and to a starting time dispersion $\tau = 200$ μs. Black diamonds represent the relative standard deviation calculated without approximation and multiplied by $\sqrt{N}$ as a function of N. Two limits are also plotted: the Cramér-Rao bounds with obstacles (dashed red line) and the min-max model where $\breve{g}$ is estimated from Eq. (11) (solid orange line).

We note that the min-max model gives an approximation of the dispersion even for small numbers N. The transition between the min-max model (where the dispersion is independent of τ) and the Cramér-Rao bound is observed for $N \approx 1000$ with $\tau = 200$ μs. Using Eq. (19), the intersection N_* of the two curves is found to be

$$N_* \simeq \frac{\langle T \rangle}{2\tau} \frac{1}{g f_{mm}}. \tag{20}$$

This equation essentially tells us that the Cramér-Rao bound is reached when the number of atoms within a delay of less than τ from the step crosses unity.

An interesting way to assess the quality of the analysis is to look at histograms of estimators shown in Fig. 8 for two different values of N (with the same parameters as in Fig. 7). When the sampling of the edge is efficient, the distribution of estimators tends to have the Gaussian shape indicated by the dashed red curves in Fig. 8. In the opposite case, the statistics tends to be given by the non-Gaussian min-max model, so that the distribution of estimators tends to fit the Laplace distribution indicated by the solid orange curves in Fig. 8. These predictions of the simple models are approximately met by the results of full simulations, with distributions for $N = 20$ and $N = 100\,000$ approaching, respectively, Gauss and Laplace shapes.

A quantitative assessment of the shape of the distribution is the kurtosis, which should be 3 for a Gauss shape and 6 for a Laplace shape. Figure 9 shows the variation of the kurtosis for the parameters corresponding to the black diamonds in Fig. 7. When the sampling of the edge is efficient (i.e., for large values of N), the distribution tends to have a Gauss shape, and the kurtosis effectively approaches 3 (dashed red line). When the statistics is, in contrast, dominated by the non-Gaussian min-max model, the distribution tends to have a Laplace shape, and the kurtosis approaches 6 (solid orange line).

We finally show in Fig. 10 the standard deviation multiplied by $\sqrt{N}$ as a function of the dispersion τ. This quantity tends to a limit independent of N for large values of τ, which

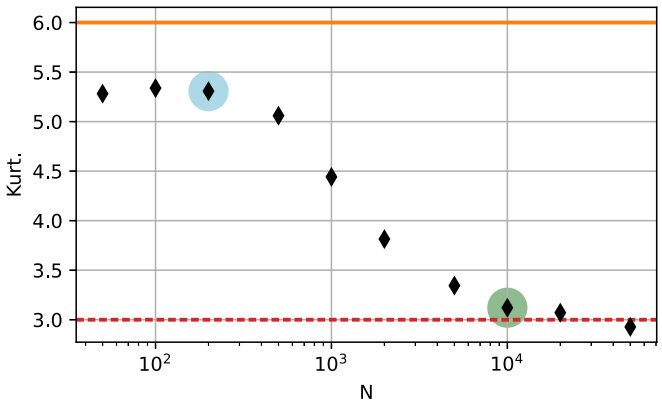

FIG. 9. Kurtosis of the histograms of $\check{g}$ in the configuration in Fig. 7, drawn as a function of N. The horizontal lines represent the limiting values of 3 and 6 obtained, respectively, for the Gauss distribution (dashed red line) and the Laplace distribution (solid orange line). Highlighted points correspond to those shown in Figs. 7 and 8.

corresponds to a statistical efficiency close to 1 and a dispersion approaching the Cramér-Rao bound. On the other hand, the Fisher information scales as $1/\tau$ for small values of τ, where the estimator is efficient only for very large values of N. For τ around 1×10^{-3} s, there is good agreement with the model in Eq. (18).

V. EFFECT OF QUANTUM REFLECTIONS

Ultracold antihydrogen atoms falling onto the detection plate suffer a quantum reflection (QR) on the Casimir-Polder potential before touching the surface, and this could affect the free-fall measurement [21,25]. As quantum reflections could change the results of the discussions presented up to now, we have repeated the analysis by taking QR into account.

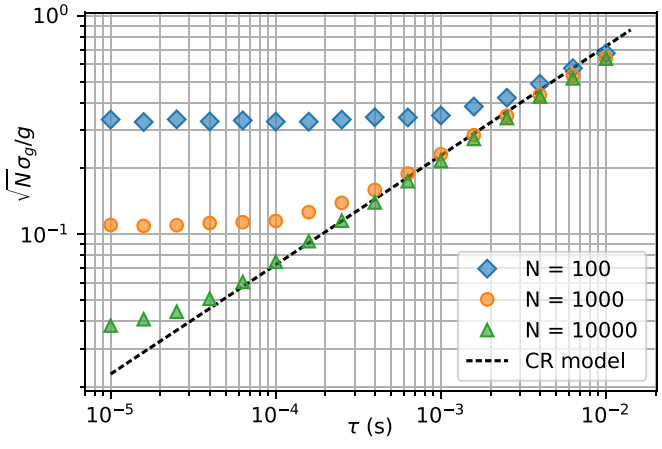

FIG. 10. Relative dispersion σ multiplied by $\sqrt{N}$ as a function of τ for different values of N. For small values of τ, this quantity tends to a finite value depending on N. For large values of τ, the Cramér-Rao bound is reached, and the quantity tends to a universal curve, meaning that σ scales as $\sqrt{\tau/N}$. The dashed line represents the Cramér-Rao limit obtained using the Fisher information given in Eq. (18).

The probability of quantum reflection on the plate depends on the component of velocity orthogonal to the plate and on the optical properties of the material. Here we assume that the boundaries of the free-fall chamber are well-polished stainless-steel plates behaving like a mirror of good optical quality. A good approximation of quantum reflection probabilities is thus obtained by taking the values calculated for a mirror that perfectly reflects electromagnetic fields [21].

For simplicity, we use an interpolation formula which was designed to reproduce accurately the full range of numerically calculated curves [26],

$$|r|^2 = \exp\left[-4\kappa/\left(1+\frac{\alpha\kappa^{2/3}}{1+\beta\kappa^{-1}}\right)\right],$$
$$\kappa \equiv k|b| = \frac{m|b|}{\hbar}|V_\perp|, \quad \alpha \simeq 0.7088, \quad \beta \simeq 0.5163. \tag{21}$$

Here k is the atomic wave vector determined by the orthogonal velocity $V_\perp$, and b is the imaginary part of the scattering length deduced from the optical properties of the surfaces. For a mirror that perfectly reflects electromagnetic fields, $|b| \simeq 28.75$ nm [27]. The constants α and β were obtained by a least-squares fit to the numerically calculated curves. Formula (21) reproduces the analytical asymptotic behaviors known at low and high energies, and it gives an estimate of the reflection probability with a relative dispersion better than 1×10^{-4} at all energies.

As different velocities correspond to neatly different probabilities, it is necessary to calculate the quantum reflection probability for each individual trajectory. Although quantum reflection probabilities are small, they can give rise to systematics of the same order of magnitude as the statistical accuracy looked for in the GBAR experiment, and it is necessary to take them into account in the analysis.

From a detection at positions $(\mathbf{R}, T)$ in space and time, we have to find the initial velocity of the trajectory. There is a one-to-one matching between those values, which, however, depends on reflections in the interval between the initial launch and detection on a surface of the free-fall chamber. Precisely, a detection point on a surface of the chamber can be reached by a direct trajectory or by a trajectory that contains one or several reflections on the disks or on another surface of the chamber. As elementary quantum reflection probabilities are small, we disregard here the case of multiple quantum reflections.

The probability current is obtained by adding the different contributions

$$J(\mathbf{R}, T) = J_{\rm dir}(\mathbf{R}, T) + \sum_{\rm surf} J^{(s)}_{\rm QR}(\mathbf{R}, T), \tag{22}$$

where $J_{\rm dir}(\mathbf{R}, t)$ corresponds to direct trajectories and each $J^{(s)}_{\rm QR}$ describes the case with one quantum reflection on the surface s. Each of the latter expressions contains the associated quantum reflection probability.

For the configuration of a cylindrical chamber with disks (with the same parameters as in the default configuration considered above), with parameters $f = 1$ MHz and $\delta E = 30$ μeV and horizontal polarization of the laser, the fraction

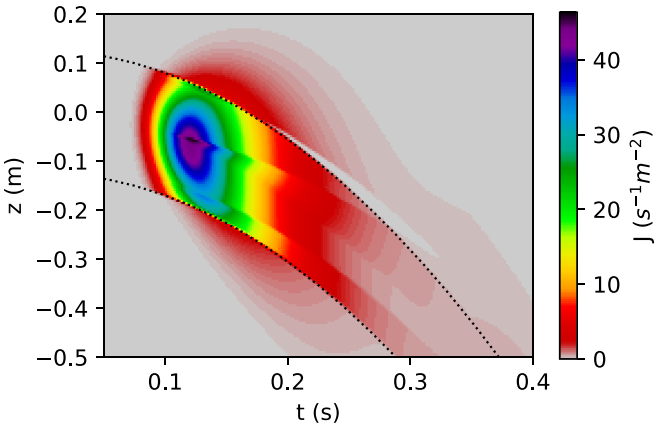

FIG. 11. Particle current J incident on the walls calculated taking into account quantum reflections. The limit of the shadow zone is represented by dotted lines.

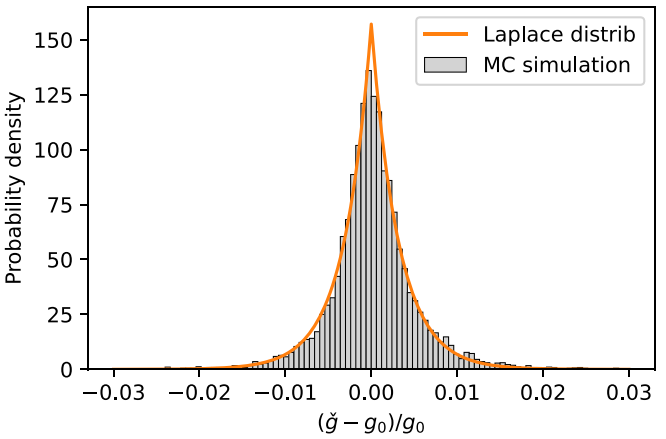

FIG. 13. Normalized histogram of 10 000 estimators $\check{g}$ obtained with quantum reflection. The parameters are the same as in Fig. 11.

of atoms that reach the surfaces of the detection chamber is about 66% (the other 34% are annihilated on the disks and are useless for the measurement of g), while ∼18% of the atoms annihilated on the surfaces of the free-fall chamber are reflected on another surface before their detection.

We represent in Fig. 11 the current on the walls as a function of time t and position coordinate z, with the choice of parameters corresponding to that in Fig. 2 except for the fact that quantum reflection is now accounted for. The essential information in the new plots is that quantum reflections allow atoms to reach the shadow zone, which was previously forbidden. We also observe that there remains a small forbidden zone which cannot be reached by any trajectory even when taking into account quantum reflections.

We repeat all steps in the calculations described in Sec. III now taking into account quantum reflections in the simulation as well as in the estimation stages.

We represent in Fig. 12 the likelihood functions calculated for random draws of $N = 1000$ $\overline{\mathrm{H}}$ atoms. We clearly see that

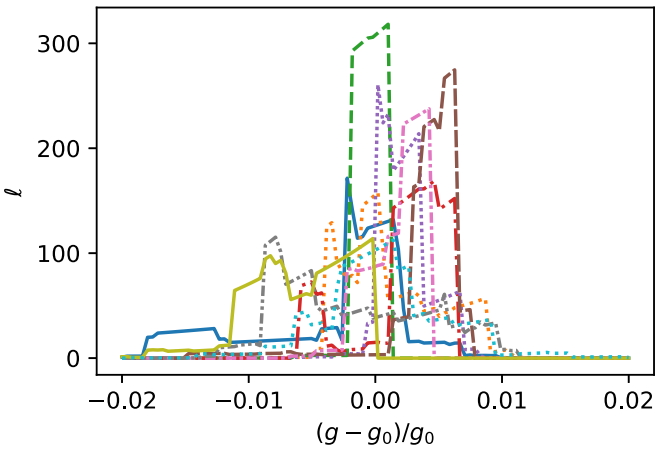

FIG. 12. Sample of normalized likelihoods including quantum reflections calculated for independent random draws of 1000 atoms. The parameters are the same as in Fig. 11.

the likelihoods are not Gaussian and contain different steps, in particular due to the interception of some trajectories by the disks. We also notice that some likelihood functions are significantly biased.

We then show in Fig. 13 a histogram of the estimator $\check{g}$ obtained by repeating the process presented in Sec. III. We deduce the average μ_g and the standard deviation σ_g of the estimators of g. The relative statistical bias $(\mu_g - g_0)/g_0$ and relative dispersion σ_g/g_0 are found to be, respectively, 0.03% and 0.54%.

As could be expected, the presence of quantum reflection degrades the dispersion, but the degradation is limited when considering that the expected relative dispersion was 0.36% with the same experimental conditions (the initial velocity distribution and parameters of the photodetachment laser) with quantum reflection not accounted for.

For completeness, we also evaluated the confidence intervals containing 95% of the probability in the histogram of the estimators $\check{g}$. We found [9.751; 9.868] for the confidence interval with no quantum reflection and [9.739; 9.891] for the confidence interval including quantum reflection. As could be expected, the confidence intervals are larger than if they were calculated for a Gaussian distribution with the known standard deviations. However, there is no significant difference in this respect associated with quantum reflection.

VI. CONCLUSION

In this paper we have studied in a detailed manner the effect of the obstacles present in the vicinity of the source on the dispersion of the free-fall acceleration measurement of $\overline{\mathrm{H}}$ atoms to be performed by the GBAR experiment. In order to ease the discussion, we have considered a clean geometry with two disks symmetrically positioned above and below the source to hide the obstacles.

We first performed Monte Carlo simulations in order to discuss the accuracy to be expected for the measurement. We showed that the accuracy is improved thanks to the additional information about the value of g gained from the presence of shadow edges, the positions of which depend on g. We have also studied the statistics of events close to an edge to obtain

a quantitative understanding of the different regimes observed for the variation of the dispersion versus the number N of $\overline{\mathrm{H}}$ atoms.

We finally took into account quantum reflection processes on the Casimir-Polder potential above matter surfaces. These processes lead to detection of $\overline{\mathrm{H}}$ atoms in the shadow zones, which could have been detrimental for the accuracy. We, however, showed that quantum reflection only slightly reduces the advantage coming from the gain of information associated with shadow edges.

ACKNOWLEDGMENTS

We thank our colleagues in the GBAR Collaboration [28] for insightful discussions, in particular F. Biraben, P. P. Blumer, P. Crivelli, P. Debu, A. Douillet, N. Garroum, L. Hilico, P. Indelicato, G. Janka, J.-P. Karr, L. Liszkay, B. Mansoulié, V. V. Nesvizhevsky, F. Nez, N. Paul, P. Pérez, C. Regenfus, F. Schmidt-Kaler, A. Yu. Voronin, and S. Wolf. This work was supported by the Programme National GRAM of CNRS/INSU with INP and IN2P3 cofunded by CNES.

[1] M. Hori and J. Walz, Physics at CERN's antiproton decelerator, Prog. Part. Nucl. Phys. **72**, 206 (2013).

[2] W. A. Bertsche, E. Butler, M. Charlton, and N. Madsen, Physics with antihydrogen, J. Phys. B **48**, 232001 (2015).

[3] M. Charlton, A. P. Mills, and Y. Yamazaki, Special issue on antihydrogen and positronium, J. Phys. B **50**, 140201 (2017).

[4] Y. Yamazaki, Cold and stable antimatter for fundamental physics, Proc. Jpn. Acad., Ser. B **96**, 471 (2020).

[5] A. E. Charman (The ALPHA Collaboration), Description and first application of a new technique to measure the gravitational mass of antihydrogen, Nat. Commun. **4**, 1785 (2013).

[6] S. Maury, W. Oelert, W. Bartmann, P. Belochitskii, H. Breuker, F. Butin, C. Carli, T. Eriksson, S. Pasinelli, and G. Tranquille, ELENA: The extra low energy anti-proton facility at CERN, Hyperfine Interact. **229**, 105 (2014).

[7] W. A. Bertsche, Prospects for comparison of matter and antimatter gravitation with ALPHA-g, Philos. Trans. R. Soc. A **376**, 20170265 (2018).

[8] D. Pagano *et al.*, Gravity and antimatter: The AEgIS experiment at CERN, J. Phys.: Conf. Ser. **1342**, 012016 (2020).

[9] B. Mansoulié (GBAR Collaboration), Status of the GBAR experiment at CERN, Hyperfine Interact. **240**, 11 (2019).

[10] P. Indelicato *et al.*, The GBAR project, or how does antimatter fall? Hyperfine Interact. **228**, 141 (2014).

[11] P. Pérez *et al.*, The GBAR antimatter gravity experiment, Hyperfine Interact. **233**, 21 (2015).

[12] T. A. Wagner, S. Schlamminger, J. H. Gundlach, and E. G. Adelberger, Torsion-balance tests of the weak equivalence principle, Class. Quantum Gravity **29**, 184002 (2012).

[13] P. Touboul *et al.*, MICROSCOPE Mission: First Results of a Space Test of the Equivalence Principle, Phys. Rev. Lett. **119**, 231101 (2017).

[14] C. M. Will, *Theory and Experiment in Gravitational Physics*, new ed. (Cambridge University Press, Cambridge, 2018).

[15] V. Viswanathan, A. Fienga, O. Minazzoli, L. Bernus, J. Laskar, and M. Gastineau, The new lunar ephemeris INPOP17a and its application to fundamental physics, Mon. Not. R. Astron. Soc. **476**, 1877 (2018).

[16] P. Asenbaum, C. Overstreet, M. Kim, J. Curti, and M. A. Kasevich, Atom-Interferometric Test of the Equivalence Principle at the 10^{-12} Level, Phys. Rev. Lett. **125**, 191101 (2020).

[17] J. Walz and T. W. Hänsch, A proposal to measure antimatter gravity using ultracold antihydrogen atoms, Gen. Relativ. Gravitation **36**, 561 (2004).

[18] O. Rousselle, P. Cladé, S. Guellati-Khelifa, R. Guérout, and S. Reynaud, Analysis of the timing of freely falling antihydrogen, arXiv:2111.02815.

[19] L. Hilico, J.-P. Karr, A. Douillet, P. Indelicato, S. Wolf, and F. Schmidt-Kaler, Preparing single ultra-cold antihydrogen atoms for free-fall in GBAR, Int. J. Mod. Phys.: Conf. Ser. **30**, 1460269 (2014).

[20] N. Sillitoe, J.-P. Karr, J. Heinrich, T. Louvradoux, A. Douillet, and L. Hilico, $\bar{\mathrm{H}}^{+}$ sympathetic cooling simulations with a variable time step, JPS Conf. Proc. **18**, 011014 (2017).

[21] G. Dufour, A. Gérardin, R. Guérout, A. Lambrecht, V. V. Nesvizhevsky, S. Reynaud, and A. Y. Voronin, Quantum reflection of antihydrogen from the Casimir potential above matter slabs, Phys. Rev. A **87**, 012901 (2013).

[22] M. Fréchet, Sur l'extension de certaines évaluations statistiques au cas de petits échantillons, Rev. Int. Stat. Inst. **11**, 182 (1943).

[23] H. Cramér, *Mathematical Methods of Statistics*, new ed. (Princeton University Press, Princeton, NJ, 1999).

[24] P. Réfrégier, *Noise Theory and Application to Physics: From Fluctuations to Information*, Advanced Texts in Physics (Springer, New York, 2004).

[25] G. Dufour, Quantum reflection from the Casimir-Polder potential, Ph.D. thesis, Université Pierre et Marie Curie, Laboratoire Kastler Brossel, 2015.

[26] G. Dufour, G. Guérout, A. Lambrecht, and S. Reynaud (private communication).

[27] G. Dufour, P. Debu, A. Lambrecht, V. V. Nesvizhevsky, S. Reynaud, and A. Y. Voronin, Shaping the distribution of vertical velocities of antihydrogen in GBAR, Eur. Phys. J. C **74**, 2731 (2014).

[28] CERN, GBAR Collaboration, https://gbar.web.cern.ch/.